A brief study on the influence of the index of revolution on the performance of Gorlov Helical Turbine

Jayaram V *‡ (iD) , Dr. Bavanish B ** (iD)

* Research scholar, Department of Mechanical Engineering, Noorul Islam Centre for Higher Education, Tamil Nadu, India

** Associate professor, Department of Fire Technology and Safety Engineering, Noorul Islam Centre for Higher Education, Tamil Nadu, India

(jayaramvijayan@gmail.com, dr.bbavanish@gmail.com)

‡ Corresponding Author: Phone: +91 9809816191, E-mail: jayaramvijayan@gmail.com

Abstract- Gorlov Helical Turbine is a helical bladed vertical axis hydrokinetic turbine generally employed to generate energy from the low-velocity currents of perennial/tidal sources. This study aims to determine the performance of NACA 4412 bladed GHTs by varying the helical blades' index of revolution. Nine turbine models with diameters of 0.6 m and heights of 0.6 m were designed with different indexes of revolution and then subjected to computational simulation. Simulation results indicate that the output power generated by the best configuration (index of revolution =0.25, P= 0.951 W) is consistent with the values derived using the analytical formula (index of revolution =0.25, P=1.11 W).). The research findings suggest that the turbine with 0.25 as the index of revolution is the best among the class. Following the earlier research findings, the helical and overlap angle corresponding to this configuration were 60^0 and 90^0, respectively. A model with 0.25 as the index of revolution was fabricated and tested at a river creek. The results were found to agree with the simulations accounting for the losses. The study's findings could promote the installation of hydrokinetic turbines in river creeks, hence enhancing SHP grid capacity in India.

Keywords Cross Flow Turbines, Gorlov Helical Turbines (GHT), Index of revolution, Computational simulation, Experimentation, Optimisation, Renewable energy.

1. Introduction

Electrification has resulted in a dramatic lifestyle alteration in every facet of modern civilisation. The increased demand for electricity has resulted in several technologies that convert energy from natural power sources to electricity [1]. The extensive use of petroleum and coal has aggrieved the effects of global warming. This has compelled many developing countries to accelerate the adoption of renewable energy technologies. The ocean and perennial sources are the most prevalent renewable energy sources (currents). Tidal energy (including perennial sources), compared with other clean energy sources such as wind, sun and geothermal, is continuous and foreseeable for the future. Hydropower is a critical renewable energy source. The immense reservoirs, seas, and river streams all have energy potential in the form of currents. Conventional turbines are ideally suited for applications requiring a low discharge with a high head or a high discharge with a low head. They are, nevertheless, ineffective in ultra-low head scenarios. Another possible location is in the tailrace of irrigation dams. Hydropower potential from such systems is frequently untapped based on perceived economic impracticality. Hydrokinetic turbines are the optimal choice for these types of energy sources. Hydrokinetic turbines do not require a reservoir or a spillway, simplifying their design and construction. Based on the direction of current and the position of the turbine axis, hydrokinetic turbines can be classified as axial or cross-flow. The rotational axis of axial-flow hydrokinetic turbines is horizontal/inclined or parallel to the current direction. Axial-flow turbines are better suited to applications like ocean currents. Contrary to axial-flow turbines, the rotational axis of cross-flow hydrokinetic turbines is always orthogonal to the incoming current. The cross-flow turbine's cylindrical feature enables it to use the channel's depth effectively. The self-starting capability of the cross-flow turbine is well-known. Vertical axis cross-flow hydrokinetic turbines and

horizontal axis cross-flow hydrokinetic turbines are the two types of cross-flow turbines. Horizontal axis cross-flow turbines are well suited for applications in shallow water.

Vertical axis cross-flow hydrokinetic turbines, on the other hand, may operate at higher depths. Two basic vertical axis cross-flow turbines are the Savonius [2] and Darrieus [3]. H-Darrieus turbines, Squirrel cage turbines, Lucid turbines, and Gorlov turbines are modified variants of Darrieus turbines.

According to the National Statistical Office's (Government of India) Energy Statistical Report - 2021, India's total renewable energy reserve is 1,097,465 MW. Small hydropower accounts for only 1.93 per cent of the reserve (21,134 MW). Small Hydel Power Plants, according to Indian norms, are those with a capacity of between 2 and 25 MW. Over the years, the contribution of small hydropower [4] towards cumulative hydropower has not changed much, owing to the reluctance to identify and adopt better technology. The best solution for this problem is to employ cross-flow hydrokinetic turbines in canal systems, irrigation dam tailraces, and smaller river streams, thereby boosting the small hydropower sector's share.

The Gorlov Helical Turbine (GHT) is a water turbine based on the Darrieus turbine's design. In GHT, helical blades of a specific aerofoil cross-section replaced the vertical blades of the Darrieus turbine. The GHT [5] is a cost-effective, environmentally friendly reaction turbine that generates hydropower from free (kinetic) and low-head (potential) water streams. Although this is a new technology, the turbine has already been deployed in several high-tide-potential coastal locations. One of the oldest operating projects is in the Uldolmok Strait of South Korea (Figure 1).

Fig. 1. GHT being installed in South Korea.

M. Gorlov [5] investigated the effectiveness of a three-bladed GHT with a diameter of 0.6096 m and a height of 0.8636 m. Gorlov employed a 0.1778 m chord- NACA0020 (National Advisory Committee for Aeronautics) aerofoil for stability. The turbine was found to have an efficiency of 35% at a flow rate of 1.54 m/s. Shiono et al. [6] investigated four versions of GHT. Each of them had a different helical blade configuration. The turbine blades' solidity was altered from 0.20 to 0.50 in 0.1 increments while maintaining a constant diameter and height (AR=1). While solidity substantially influenced starting characteristics, the blade inclination angle had no such effect. The turbine with a solidity of 0.4 had the maximum efficiency.

Talukdar et al. [7] investigated the performance of the GHT based on the solidity ratio. Talukdar et al. field-tested the turbines in an open channel. They found that the turbine with a solidity ratio of 0.38 at a TSR of 1.02 developed a maximum power coefficient of 0.20 at a velocity of 0.87 m/s. Additionally, the influence of the solidity ratio on the turbines' performance was investigated at various immersion levels. The power coefficient was observed to decrease as the immersion depth decreased. This impact was particularly noticeable in turbines with a low solidity ratio (σ=0.31).

Pongduang et al. [8] studied the impacts of the helical angle on the GHT's performance. In a towing tank, two tidal turbines with diameters of 0.5 m and 0.6 m (height = 1.25 m) were tested. The blade's profile was NACA0020 (0.07 m chord length). Three-bladed models with helical angles of 150^0, 135^0, and 120^0 were tested under a spectrum of flow conditions. According to the studies, the model with a helical angle of 135^0 functioned well for TSR bandwidth of 2.2 to 2.5.

BK. Kirke [9] investigated the impact of pitch angles on hydrokinetic cross-flow turbines with straight and helical blades. It is well established that pitch variation improves starting torque and efficiency. However, only two pitch values were investigated (5^0 and 10^0). According to studies, the 10^0-pitch turbine had a C_p(max) of roughly 0.4.

Mosbahi et al. [10,11] investigated the performance of the Darrieus turbine with delta blades numerically and experimentally. The performance of the turbine was quantitatively assessed in context with the leading-edge sweep angles from 10^0 to 40^0. Experiments were conducted to validate the best findings (leading-edge sweep angle=30^0). The current article's numerical methodology is based on Mosbahi et al. [10,11] and Shashikumar et al. [12-14].

This literature survey indicates that various experimental and computational investigations on the GHT have been conducted to determine its performance using C_P, C_T, and solidity ratios. However, the effects of helical angle and pitch of the blade are not well assessed. Pongduang et al. [8] conducted the only study on the helical angle, focusing exclusively on 120º, 135º, and 150º. Similarly, the survey by BK. Kirke [9] on the pitch of the turbine blade is also confined to two specific values (5^0 and 10^0). U. Divakaran et al. [38] investigated the influence of helical angles (ranging from 60º to 90º) on the performance of helical VAWT (Vertical Axis Wind Turbine) numerically. The turbine's diameter and height were 2.7 and 3 m, respectively. The performance of a 60º helical VAWT was said to exceed all other VAWT blade designs and peaked at a lower TSR. U. Divakaran et al. also concluded that wakes for non-straight blade VAWTs diminish rapidly. Philip Marsh et al. [38] investigated the effects of blade overlap angles and sectional inclination angles on the performance of GHT. The output

power, torque oscillations, and mounting force were calculated for turbines with overlap angles (refer to figure 4) ranging from 0^0 to 120^0 and section inclination angles ranging from -15^0 to 45^0. The results showed that straight-bladed turbines with no blade overlap produced the most power.

The present research recommends analysing the turbine's performance using the 'index of revolution,' which is a function of the helical profile's pitch and angle. Section 2 expands on the notion of the index of revolution. The present study examines GHTs numerically by altering the index of revolution under identical flow conditions. A prototype GHT with optimal parameters is fabricated and experimentally confirmed following simulation recommendations. The following are the study's objectives:

(i) To study the performance of a GHT numerically and experimentally at various revolution indices (0.1 to 0.5 with a 0.05 increment).

(ii) To find out the optimum configurations of GHT in terms of helical and blade overlap angle.

2. Index of Revolution

The study investigates the parametric optimisation of GHT with respect to the Index of revolution [15] and further a methodology to implement them in a perennial/tidal source. Even though there are various parameters to be optimised, such as helical angle and solidity ratio [16], the effort has been concentrated on the helical blade profile's index of revolution (pitch). Index of revolution may be defined as the fraction of the pitch of one complete helical turn measured parallel to the axis and fitted between the turbine discs (refer to Figure 2, 4).

A 3-D model [17] was created using SolidWorks and subjected to the cross-flow velocity of 1.5 m/s. Since a helical cross-flow turbine is known for its automated self-starting capability, no rudders were provided. The parameters governing [18] helical turbine design include the radius of the disc, blade cross-sectional geometry (profile), helical-pitch angle, aspect ratio, number of blades, solidity ratio and design of strut. The study concentrated on the revolution index (pitch) in this research work. The Index of revolution was incremented by a value of 0.05 until half of the total revolution of the helix was reached. In all cases, the pitch of the helix had to be decreased to readjust the model's geometry (height being fixed to 0.600 m). Details of the geometric configuration of GHT in terms of the Index of revolution are given in Table 1. Further details regarding Centre of Gravity (CG) and Moment of Inertia (MOI) are provided in Table 2.

As indicated by equation 1, the Index of revolution is defined as the ratio of the turbine's height to the pitch of the helical blades. In other words, the Index of revolution can be defined as the percentage of helical pitch that will be considered for the turbine (refer to Figure 2).

Index of revolution = (Height of turbine, H / Pitch of helical blades, P)   (1)

Table 1 indicates how parameters such as helical angle, overlap angle and enwinding ratio are related to indices of revolution. The pitch angle that the helical blade makes with a horizontal plane is referred to as the helical pitch angle or helical angle (φ). The plane angle generated by the cross-section of a single blade projected on the top of the blade to the bottom plane is the blade overlap angle (β). The Index of revolution, helical angle and blade overlap angle are illustrated in figure 4. The enwinding ratio is a metric that measures the helicity of helical blades and is computed using equation 2.

Enwinding ratio = (Number of blades, N x blade overlap angle, β / 360)   (2)

The higher the enwinding ratio, the greater the helicity is. The enwinding ratio is usually less kept below two for an efficient design. The blade element distribution will be more uniform if the enwinding ratio is near a positive integer.
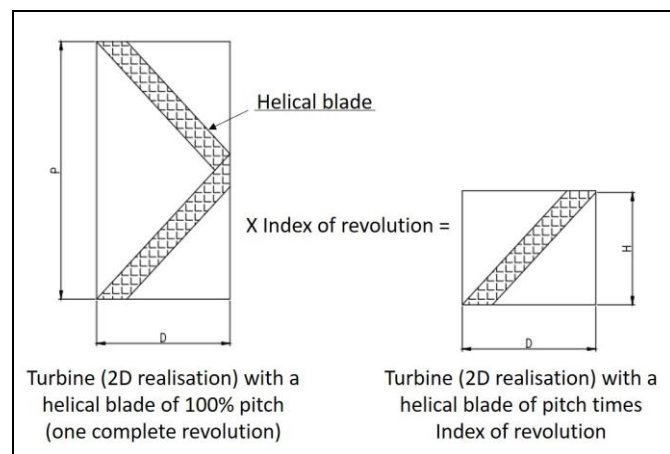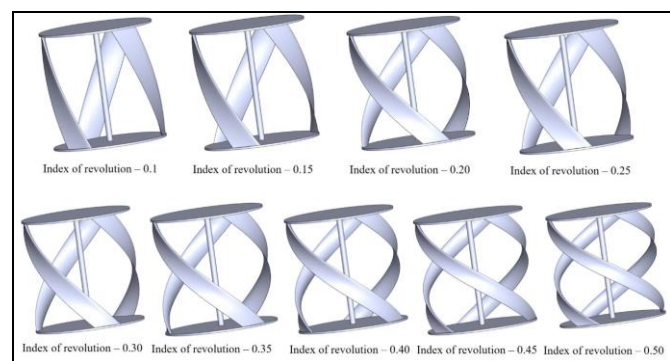

Fig. 2. Concept of index of revolution.

Fig. 3. GHTs with different indices of revolution.

Table 1. Geometric configuration of GHT in terms of Index of revolution

Height of the turbine, H (m)	Pitch of the helix, P (m)	Index of revolution = (H/P)	Helical angle, φ	Overlap angle, β	Enwinding ratio
0.600	6.000	0.10	73.21	36	0.30
	4.000	0.15	65.08	54.02	0.45
	3.000	0.20	62.12	71.98	0.60
	2.400	0.25	60.00	90.11	0.75
	2.000	0.30	51.21	108.13	0.90
	1.714	0.35	44.32	126	1.05
	1.500	0.40	41.52	143.92	1.20
	1.333	0.45	36.12	162.08	1.35
	1.200	0.50	33.27	180	1.50

Table 2. CG and MOI of GHT in terms of Index of revolution

Index of revolution	Mass (kg)	CG (m)			MOI I_{zz} (kg m^2)
		X	Y	Z	
0.1	30.99	0	0	0.31	2.79
0.15	30.99				
0.2	30.99				
0.25	30.97				
0.3	30.98				
0.35	31.00				
0.4	31.00				
0.45	30.99				
0.5	30.98				
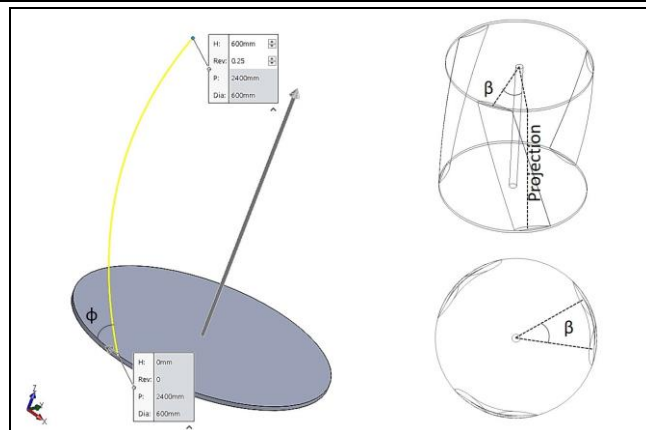
Fig. 4. Blade trajectory, helical angle (φ) and blade overlap angle (β) of turbine with 0.25 as the index of revolution.

3. Design of GHT (Analytical Model)

As recommended in the literature and experiment [19], the number of blades was determined to be three. The NACA 4412 blade profile with a 0.120 m chord was adopted, unlike previous studies While S1210 looks to have an advantage over NACA 4412 in performance, it is more complex to fabricate. Figure 5 compares the several standard profiles used for the purpose mentioned earlier. The helical sweep is typically three times the height of the turbine. For example, a turbine with a height of 0.600 m would have a helical sweep height of 1.800 m.
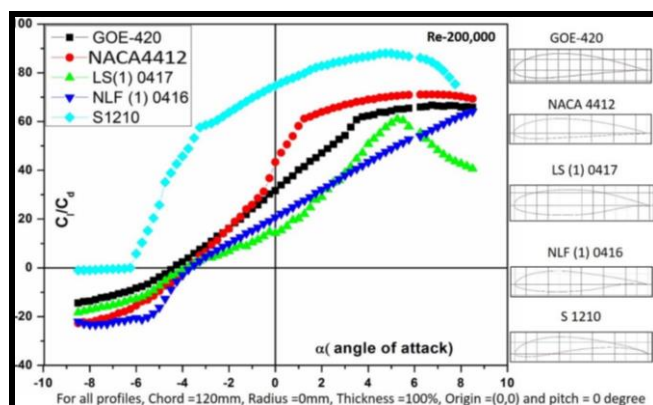

Fig. 5. Comparison of various aerofoil profiles of GHT

During the initial part of the investigation, a series of simulations by varying heights was undertaken to determine the optimal height. The turbine's height was switched between 0.500 m and 0.900 m in a step size of 0.050 m. (9 Models). The model with a 0.600 m height outperformed the others in terms of torque. Following that, nine Gorlov Helical Turbines with a diameter of 0.600 m and a height of 0.600 m were modelled. Each model had a unique revolution index (starting from 0.10 and ending with 0.50, refer to Figure 3). Additional simulations with input flow velocities ranging from 1.1 m/s to 1.7 m/s were performed for all turbines with indices of revolution (0.10 to 0.50) to establish the correlation between power coefficient and TSR. The Gorlov turbine's physical/analytical calculations are as follows. The turbine's most often utilised geometrical property is its relative solidity, expressed as the ratio

$$\sigma = \frac{nb}{D} \tag{3}$$

The solidity ratio indicates the proportion of the turbine's diameter that is solid compared to the entire circumference. In short, it refers to the effective frontal area resisting the fluid. The solidity ratio is often employed to find the tangential force acting on the turbine. M. Gavasheli [19] derived an equation to evaluate the solidity ratio in blade area projections on the turbine shaft plane. Indicating the helical turbine's solidity by P (in terms of blade projection on the lateral plane),

$$P = \frac{2nHr}{\pi}(d + \sum_{j=1}^{n}\sin(\frac{j\pi}{n} - d) - \sin\frac{j\pi}{n}) \tag{4}$$

The relative solidity of the turbine σ = P/2Hr is calculated as follows:

$$\sigma = \frac{n}{\pi}(d + \sum_{j=1}^{n}\sin(\frac{j\pi}{n} - d) - \sin\frac{j\pi}{n}) \tag{5}$$

For example, for a four-blade turbine configuration, the relative solidity would be:

$$\sigma = \frac{4}{\pi}(d + \sin(\frac{\pi}{4} - d) - \sin\frac{\pi}{4} + \sin(\frac{\pi}{2} - d) - \sin\frac{\pi}{2}$$
$$+ \sin(\frac{3\pi}{4} - d) - \sin\frac{3\pi}{4} + \sin(\pi - d) - \sin\pi) \tag{6}$$

Further simplification of the equation involves incorporating the value of 'd' in terms of the chord (in radians). The authors opted for a triple-blade configuration due to its self-starting characteristics, and hence the expression for relative solidity is:

$$\sigma = \frac{3}{\pi}(d - \sqrt{3} + \sin d + \sqrt{3}\cos d) \tag{7}$$

Further, in order to find the tangential force on the turbine the following formula is employed:

$$F = \frac{1}{2}C_d\rho\sigma AV^2 \tag{8}$$

The force is partially due to pressure exerted by the moving fluid on the projected area estimated with a relative solidity ratio. The torque is calculated according to equation 9.

$$T = 0.5FD \tag{9}$$

As indicated above, formulas are used for the tangential drag force, torque, and power developed by the turbine. A primary study on the tangential force of the turbine blades was made for a whole set of parameters, including turbine, blade chord length, etc. Knowing the value of the Tip Speed Ratio (TSR), the turbine's angular/rotational velocity can be estimated as:

$$\omega = \frac{2V\lambda}{D} \tag{10}$$

The power of the turbine can be estimated using the idealistic formula:

$$P_{ideal} = T \times \omega \tag{11}$$

However, in actual practice, the shaft power of the turbine and the final output will be further reduced due to mechanical transmission losses, gearbox efficiency (η_m) and generator efficiency(η_e). The equation can be modified according to equation 12.

$$P_{actual} = C_p\eta_m\eta_e P_{ideal} \tag{12}$$

The coefficient of power in the above equation can be estimated using:

$$C_p = \frac{T\omega}{\frac{1}{2}\rho\sigma AV^3} \tag{13}$$

The Tip Speed ratio can be estimated using:

$$TSR = \frac{\omega R}{V_f} \tag{14}$$

The model meant for simulation and experimentation had 0.120 m chord length and 0.600 m height. The TSR had a value of 1.00 for sampling measurements (usually varied between 0.5 & 2.5).

The density of the fluid flowing across the turbine, ρ=1000 kg/m³

The velocity of fluid flow, V_f=1.5 m/s

Number of helical blades in the turbine, N=3

The chord length of the blade, c=0.120 m

The turbine diameter, D=0.600 m

Half of the blade's chord length measured in radians with respect to the axis of rotation is given by:

d=c/D=0.2 rad

For a turbine with three blades, the relative solidity is given by:

$$\sigma = \frac{3}{\pi}(\frac{1}{5} - \sqrt{3} + \sin(\frac{1}{5}) + \sqrt{3}\cos(\frac{1}{5})) = 0.1943$$

This implies that a flow resistance is made available by 19.43 % of the overall estimated turbine's frontal area. The turbine height, H = 0.600 m. The frontal area of the turbine without considering relative solidity, A= H x D = 0.360 m^2

An unsymmetrical aerofoil -NACA 4412 was considered for the profile of the helical blades, as mentioned in section 3.

The drag coefficient (average), $C_{d\ avg}$=0.03627

Recalling Equation (8), the tangential force on the turbine:

$$F = \frac{1}{2}C_d \rho \sigma A V^2 = 2.85N$$

For a TSR (λ) = 1.00, the angular velocity of the turbine is estimated as:

$$\omega = \frac{2V\lambda}{D} = 5 rad/s$$

Turbine power, $P_{ideal} = F \times \omega \times \frac{D}{2} = 4.275W$

Due to mechanical transmission losses, gearbox efficiency, and generator efficiency, the turbine's shaft power and final output would be reduced even further (refer to equation 12). The standard estimate is 25%. The actual power is:

$P_{actual} = 1.11$ W

4. Simulation

4.1 Development of part geometry for simulation

The blades of the GHT are modelled using the helical profile available in the SolidWorks modelling package. The spatial points for NACA 4412 with a chord length of 0.12 m are generated via an open-source web module (www.airfoiltools.com). The maximum and minimum values of blade thickness and camber are used to compute the aerofoil's spatial points, as shown in Figure 6. After that, the aerofoil profile (NACA 4412) [22] is etched onto the GHT's bottom disc. The inclination angle of the sectional blade and the angle of attack are arbitrarily fixed to zero. The sweep profile characteristic is employed to create the helical blades' requisite trajectory, as depicted in Figure 7 A.

At this stage of the modelling, the height and index of the turbine's revolution can be adjusted (refer to Figure 7 B). As illustrated in Figure 7 C, a parallel plane is projected at the desired height. This plane is used to create the second disc, which has the same diameter as the first (refer to Figure 7 D). The remaining two blades are modelled using the circular

pattern feature (refer to Figure 7 E). The axis of reference was set as Z (local). Figures 7 F illustrates the completed geometry.
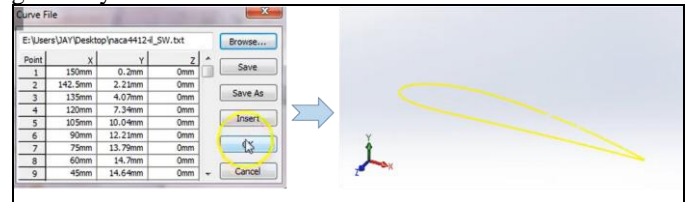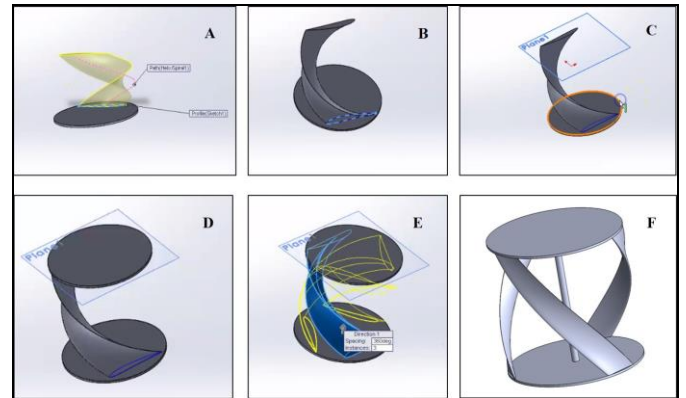

Fig. 6. Profile generation using Solid works

Fig. 7. Various stages in modelling GHT

Figure 8 depicts the front view of GHT, highlighting essential geometric elements such as height (H), diameter (D), and helical blades.
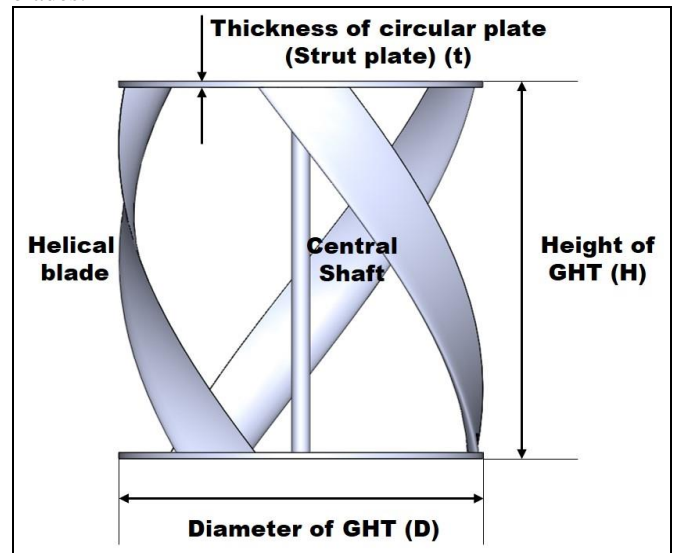

Fig. 8. 3-D model of the GHT with all geometric parameters (front view)

4.2 Computational domain for finite volume.

The 3-D computational domain modelled similar to an open channel of a river stream and simulated using SolidWorks Flow Simulation Module (FSM) [26-31] is shown in Figure 9. The computational domain is bounded on all sides by four walls: bottom, left, right, and a top surface open to the atmosphere. The overall length of the

computational domain (from inlet to exit faces) is set to five times the diameter of the GHT (5D) [23]. The GHT is placed at the centre of the computational domain (2.5 times its diameter (2.5D) away from the computing domain's inlet and exit).
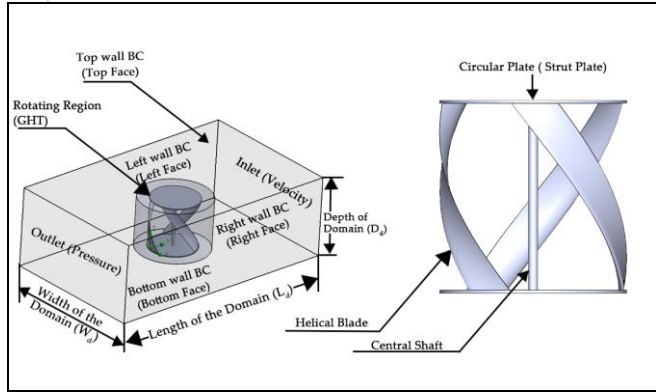

Fig. 9. Details of the computational domain and rotating region

The computational domain is divided into GHT, rotating area (turbine enclosure), and outer fluid region (river stream). The breadth of the domain is set to three times the GHT's diameter (3D). The axis of the GHT is equally spaced from both sidewalls (in the lateral direction). According to the literature [23-25], the rotating zone in the simulation was decided as 1.5 times the diameter of the GHT. The following Table 3 summarises the primary computational domain dimensions [23-25], including the width (W_d), length (L_d), depth (D_d) of the turbine, turbine diameter (D), and rotating region diameter (D_r).

Table 3. Details of dimensions of the computational domain and GHT

Parameter	Value
Diameter of GHT, D	0.6 m
Height of GHT, H	0.6 m
Aspect Ratio, AR	1
Length of the domain, L_d	3 m
Depth of domain, D_d	1.0 m
Width of the domain, W_d	1.8 m
Diameter of the rotating	0.9 m

4.3 Details of mesh used for computation.

The solver allocates the computational domain and essential features to a hexahedral mesh by default, as SolidWorks FSM does not allow 'orphan meshes'. The rotational and outer areas are assigned with a fine mesh, while the outer region is assigned with a coarse mesh. Hexahedral (or quad) meshes are usually more economical for wall-bounded flows due to the conservation of orthogonal grids in the wall-normal direction [27]. Hex elements are

more accurate since the angle between adjacent sides may be kept close to 90º. When the Reynolds number is large, it is necessary to be extremely precise with the spacing in the wall-normal direction. Hex grids provide for optimal wall-normal spacing while avoiding significant face skewness. In order to minimise mesh distortion along the curved surface, the refinement level is set to the maximum level of 5 (near the rotating region). Meshes have a maximum size of 1×10^{-3} m, a minimum size of 1.653×10^{-5} m, and an average size of 0.8368×10^{-3} m, respectively. For the current scenario, the y+ value is 0.9879. (Less than one). The aspect ratio and Jacobian ratio of the mesh are 1 and 4. These figures are within acceptable limits [26,27, 32]. Figure 10 depicts the meshed computational domain, the rotating area, and the inflation layer.
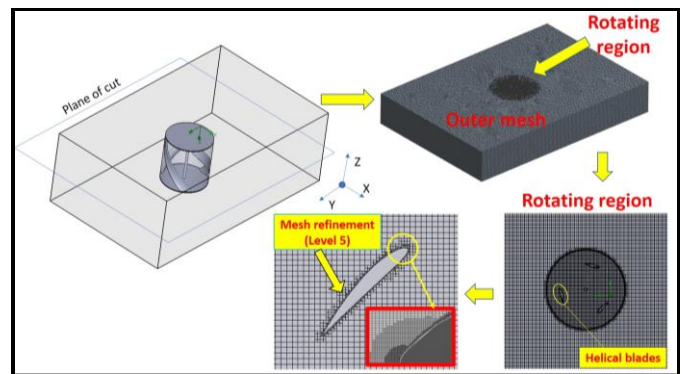

Fig. 10. Details of mesh, rotational region and mesh refinement.

4.4 Mesh independence study

The effect of the number of mesh elements on the turbine's performance index (coefficient of power, C_p) was investigated using simulations for a flow velocity of 1.5 m/s. [5-15]
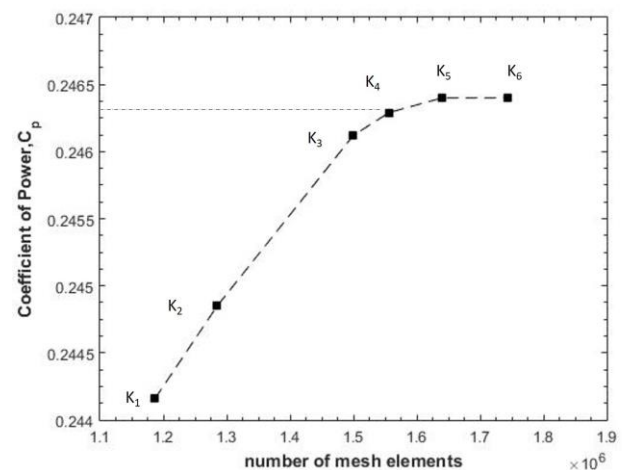

Fig. 11. Mesh independency study (variation of C_p with respect to the number of mesh elements)

The turbine with an index of revolution of 0.25 was opted for the study. Six mesh models: K_1, K_2, K_3, K_4, K_5, and K_6 with mesh elements (1,186,922); (1,285,109); (1,499,780); (1,556,050); (1,639,761); and (1,743,910) respectively were subjected for the mesh independency study. In Figure 11, the

833

power coefficient of GHT is plotted against the number of mesh elements. A closed-form solution of $C_p = 0.2463$ was utilised for the error estimation, which corresponded to the criterion described above [10-15]. When the number of mesh elements was raised beyond K_4, there was no noticeable variation in the value of C_p (refer to figure 11). The meshing models K_4 and K_5 have the lowest error values, as shown in Table 4. The K_4 mesh model was employed to maximise the efficiency of the numerical studies.

Table 4. Configuration of mesh models

Mesh model	Number of mesh elements	C_p	Error percentage	Computation time (hh:mm:ss)
K_1	118692	0.24416	0.9006	05:12:17
K_2	128510	0.24485	0.2129	05:57:07
K_3	149978	0.24612	0.1041	06:41:37
K_4	155605	0.24629	0.0327	07:07:41
K_5	163976	0.24639	0.0332	07:57:34
K_6	174391	0.24639	-	08:34:06

4.5 Governing equation and turbulence modelling

SolidWorks FSM is a parametric flow simulation tool that uses the finite volume method (FVM) to calculate a product's performance. The Navier-Stokes (NS) equations, which are representations of the mass, momentum, and energy conservation rules, are solved by the FSM in fluid domains (Equations 15-17).

$$\Delta \bullet (\bar{\rho}\bar{V}) = 0 \tag{15}$$

$$\bar{\rho}(\bar{V} \bullet \nabla)\bar{V} = -\nabla \bar{p} + \mu \nabla \bullet (\nabla \bar{V} + \bar{\rho}(\bar{V} \bullet \nabla)\bar{V}^T) - \frac{2}{3}\mu \nabla(\nabla \bullet \bar{V}) + g(t) \tag{16}$$

$$\bar{\rho}(\bar{V} \bullet \nabla)(c_V \bar{T}) = K\nabla^2 \bar{T} - p(\nabla \bullet \bar{V}) + \mu\phi + g(t) \tag{17}$$

SolidWorks FSM is devoted to the simulation of turbines (in which the flow is often turbulent). The two-equation model is one of the most frequently used turbulence models. FSM employs the K-ε model in the two-equation model [26]. The effects of both laminar and turbulent flows are considered. The flow becomes turbulent when the Reynolds number exceeds a predefined critical point. K-ε is not known to be reliable in the cases of large adverse pressure gradients. Hence the Favre-averaging is employed. The Favre-averaged NS equations are used to anticipate turbulent flows, which take into account the time-averaged effects of turbulence on the flow parameters while disregarding large-scale, time-dependent events. This method brings new elements (Reynolds stresses) into the equations. To solve this set of equations, FSM uses the turbulent kinetic energy and its rate of dissipation.

$$\frac{\partial(\rho k)}{\partial t} + \frac{\partial(\rho k u_i)}{\partial x_i} = \frac{\partial}{\partial x_j}\left[\frac{\mu_t}{\sigma_{k1}}\frac{\partial k}{\partial x_j}\right] + 2\mu_t \xi_{ij}^2 - \rho\xi \tag{18}$$

$$\frac{\partial(\rho\xi)}{\partial t} + \frac{\partial(\rho\xi u_i)}{\partial x_i} = \frac{\partial}{\partial x_j}\left[\frac{\mu_t}{\sigma_{\xi1}}\frac{\partial \xi}{\partial x_j}\right] + 2.88\frac{\xi}{k}\mu_t\xi_{ij}^2 - 1.92\rho\frac{\xi^2}{k} \tag{19}$$

Equations (18) and (19) are the conservation equations of K and ε, respectively, where σ_{K1} and $\sigma_{\varepsilon1}$ are constants with values of 1.00 and 1.30. Based on the hydraulic diameter and Reynolds Number, the turbulence intensity (I_t), turbulence length scale (l), turbulent kinetic energy (K), dissipation rate (ε) was quantified using equations 20-23:

$$I_t = 0.16 \times (\text{Re})^{-\frac{1}{8}} = 0.0304 \tag{20}$$

$$l = 0.07 \times (\text{Re}) = 0.027 \, \text{m} \tag{21}$$

$$K = \frac{3}{2}(\text{V} \times I)^2 = 3.11904 \times 10^{-3} \tag{22}$$

$$\varepsilon = C_\mu^{\frac{3}{4}} \times \frac{K^{\frac{3}{2}}}{l} = 1.06 \times 10^{-3} \, m^2/s^3 \tag{23}$$

Where $C_\mu = 0.09$ (empirical constant). These data were employed in formulating the simulation model.

4.6 Methodology

The meshed model was imported to the FSM. SI units were used for the whole system. The type of analysis was input 'internal' (meaning: Internal flow). The 'exclude cavity without flow separations' function is turned on. The rotational region was defined. Water was set as the fluid under the domain of liquids. From the 'flow characteristics' menu, the flow type was set as a mix of laminar and turbulent, excluding the effect of cavitation. The default wall for the thermal condition was set as adiabatic with roughness at zero micrometres. The velocity component along the Y direction was specified as 1.5m/s (along the length of domain, refer to Figure 9). Since the flow was set parallel to Y-axis, all components of gravity except the Z direction (refer to Figure 9) were set to zero. All velocity components (relative to rotating frame) except Y were set as zero. Equations 20-23 mentioned that the turbulence parameters were input into the solver. The boundary conditions of the inlet, outlet and side walls were inserted into corresponding fields. The fluid velocity ($V_f = 1.5$ m/s) indicates the inlet boundary condition. 'Environmental pressure' is stated as the output boundary condition. No-slip boundary criteria were provided for the side walls. All necessary parameters, such as the force on blades, angular velocity, and the torque of the turbine, were selected under the 'goals' menu in the pre-processing operations.

5. Experimentation

5.1 Fabrication of model

The model's basic structure was fabricated using a Cold Rolled (CR) iron sheet (refer to Figure 12 A). As per the best output of the simulation (index of revolution=0.25), it was decided to keep the turbine's height at 0.600 m and diameter at 0.600 m. The chord length of the blade profile was 0.120 m. The blade's profile was NACA 4412. A bicycle dynamo generator (12 V rated) was connected to the turbine shaft using suitable bearings. The structure of the model was fabricated, keeping the mean camber line of the aerofoil as a reference. Parallel lines were drawn perpendicular to the skeleton blade's edges at regular intervals. The blade pitch angle and angle of attack of the helical blades were arbitrary set as zero. A series of points on the above-mentioned line was established, and ice cream sticks with the requisite heights were glued at these locations to create an aerofoil-like curve (Figure 12B). Sealants were utilised to fill the area between the ice cream sticks (Figure 12C). The excess sealant was sanded after it had dried for a day. The ice cream sticks were wrapped with twine thread. The yarn was coated with an adhesive binder (Figure 12D). A chromium-based primer (paint) coating was provided to strengthen the turbine's corrosion resistance, as shown in Figure 12E. Finally, the second coat of paint was added to the turbine to make it more durable (Figure 12F). The turbine is enclosed in a housing structure for convenient manoeuvrability.

Fig. 12. Various stages of manufacturing GHT

5.2 Test rig

The experimental test ring included GHT, Multimeters, Dynamo, and Housing, as shown in Figure 13. A computerised laser-guided tachometer was used to measure the rpm. The voltage and current of the dynamo were measured using multimeters (Metravi P11) installed on the upper side of the turbine casing. Ropes were used to secure the test rig in place, which was then removed. Throughout the experiment, plastic covers were utilised to keep the multimeters from becoming wet.
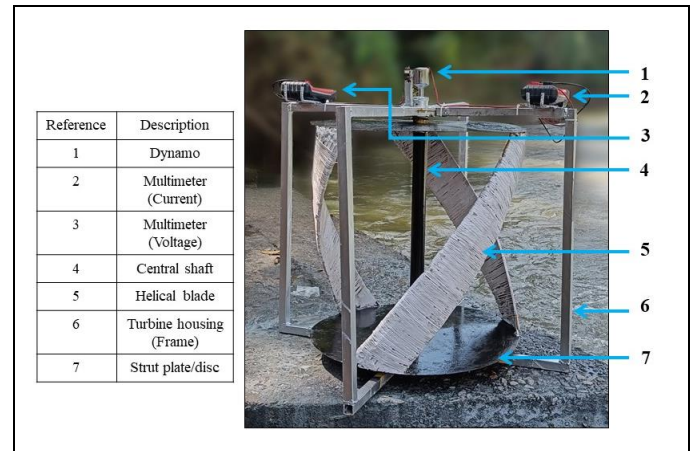

Reference	Description
1	Dynamo
2	Multimeter (Current)
3	Multimeter (Voltage)
4	Central shaft
5	Helical blade
6	Turbine housing (Frame)
7	Strut plate/disc

Fig. 13. Schematic illustrations of the test setup for GHT

5.3 Field testing and site selection

For field testing of the GHT, a suitable stream of the Karamana river was chosen (refer to Figure 14). A check dam meant as a reservoir for the pumping station for irrigation is located here. The discharge and water velocity at the state-owned water pumping station have been recorded every year. This data was used for the timing of the experiment. The rate of the stream was measured using a current metre (Nixon 4O4, Propeller type). The check dam permits a proper average depth of 0.65 m in the reservoir, which is sufficient for submerging the GHT. The check dam's upstream width is 34.56 m and spans 38.25 m. The turbine was 11 m upstream (reservoir) from the check dam, with a stream velocity of 1.5 m/s. The output power of the turbine was computed using the collected data. Table 5 shows the GHT experimental data.
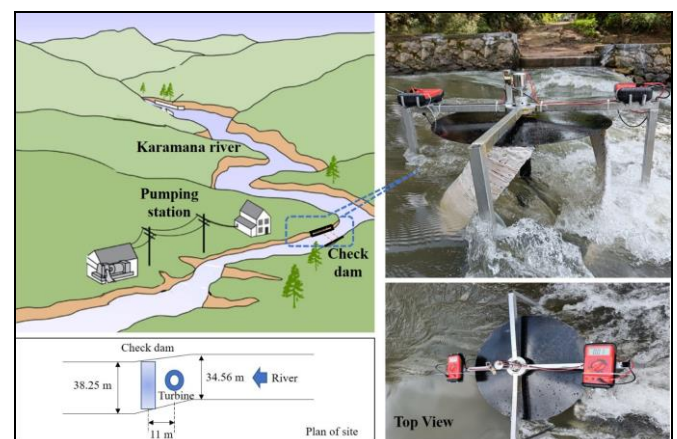

Fig. 14. Field testing and installation of GHT

Table 5. Data from experimentation

Index of revolution	Run number	Current (A)	Voltage (V)	Power (W)	RPM
0.25	1	0.13	6	0.78	51
	2	0.12	5	0.60	50
	3	0.10	6.1	0.61	49
	4	0.11	5.9	0.64	51

6. Uncertainty analysis and systematic error

Equations 24 and 25 are used to compute the uncertainty. These equations were calculated using Moffat's method [33], and the output power measurement error was found to be 2.68 %.

$$P = VI \tag{24}$$

$$\frac{\partial P}{P} = \left[\left(\frac{\partial V}{V} \right)^2 + \left(\frac{\partial I}{I} \right)^2 \right]^{\frac{1}{2}} \tag{25}$$

The systematic error associated with the various measurement equipment investigated in this study is summarised in Table 6. All of the error values and uncertainties were within the acceptable range.

Table 6. Systematic error of measuring instruments

Experimental apparatus	Systematic error
Digital Multimeter (current measurement)	0.27 %
Digital Multimeter (voltage measurement)	0.10 %
Digital tachometer (laser based, non-contact)	3 %
Current meter	1 %

7. Results

7.1 Results from simulation

Nine GHTs with a unique index of revolution were treated to a 1.5 m/s flow velocity at the input. Table 7 summarises the output characteristics of the nine GHTs designed with different indexes of revolution (0.10-0.50). The first two columns (from left to right) reflect the flow velocity and index of revolution. These are the simulation model's input parameters. The following columns (columns 3-6, from left) represent the simulation model's output parameters. These include the GHT's rotational velocity, the force acting on the helical blades, the torque produced, and the GHT's output power. The GHT with an index of revolution of 0.25 clocked the maximum output power of 0.951 W for a flow velocity of 1.5 m/s.

7.1.1. Variation of Cp (coefficient of power) with respect to TSR (Tip Speed Ratio)

The efficacy with which a hydrokinetic turbine converts the energy contained in the water to output power is indicated by the coefficient of power (C_p refer to equation 13). The Tip Speed Ratio is another critical metric for describing the turbine's performance (TSR, refer to equation 14). TSR is the ratio of the tangential velocity of the turbine blade to the flow velocity of the stream. The variation of C_p versus TSR is depicted in Figure 15(A-J).
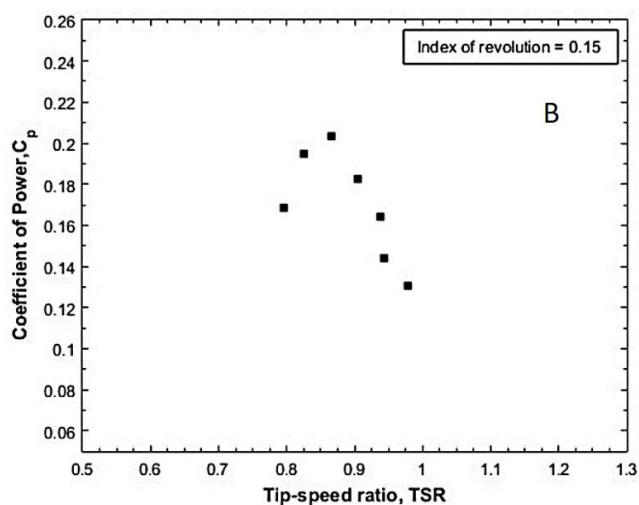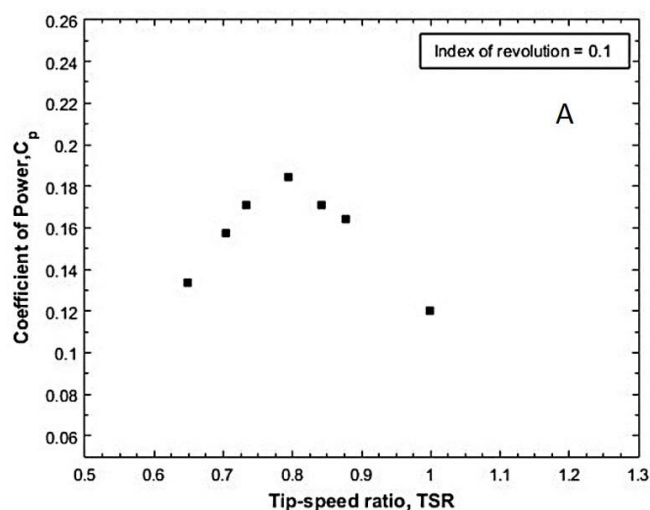
Table 7. Output characteristics of Gorlov Helical Turbine

The flow velocity of the fluid at the inlet (V_f) (m/s)	Index of revolution	Angular velocity of GHT (rad/s)	Force on GHT blades (N)	The torque generated by GHT (Nm)	Output power (W)
1.5	0.10	0.822	0.614	0.638	0.524
	0.15	0.892	0.723	0.706	0.630
	0.20	0.887	0.921	0.823	0.730
	0.25	0.902	1.758	1.055	0.951
	0.30	0.898	0.932	0.714	0.641
	0.35	0.914	0.921	0.788	0.721
	0.40	0.882	0.736	0.622	0.548
	0.45	0.826	0.526	0.602	0.497
	0.50	0.842	0.514	0.542	0.456
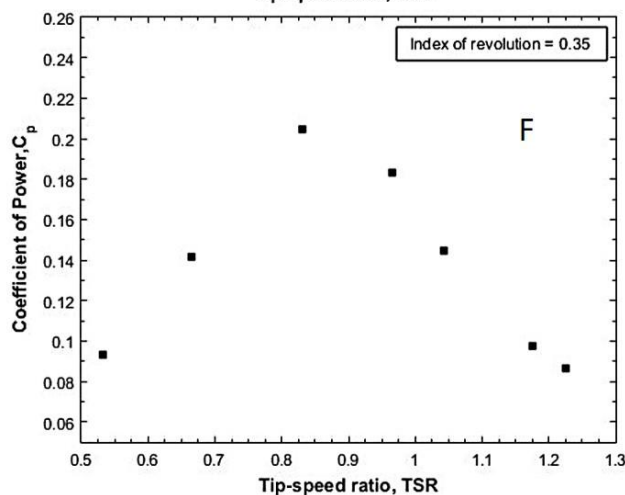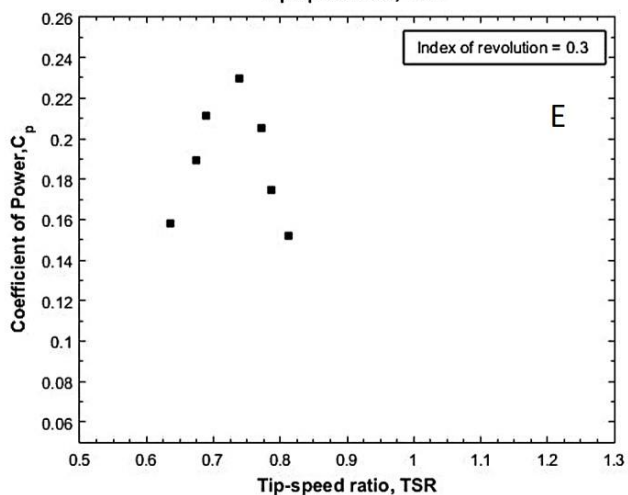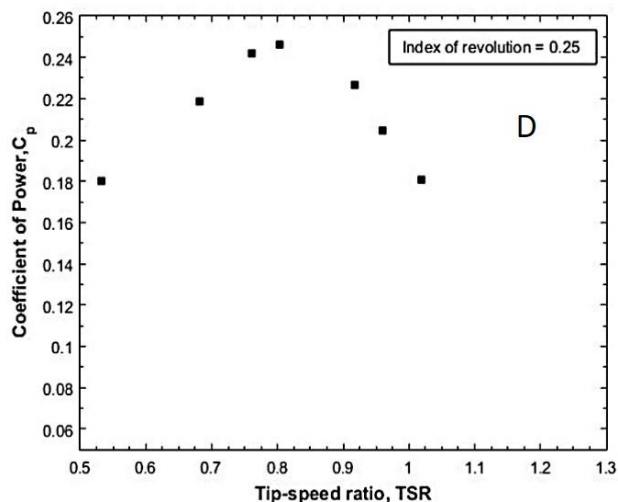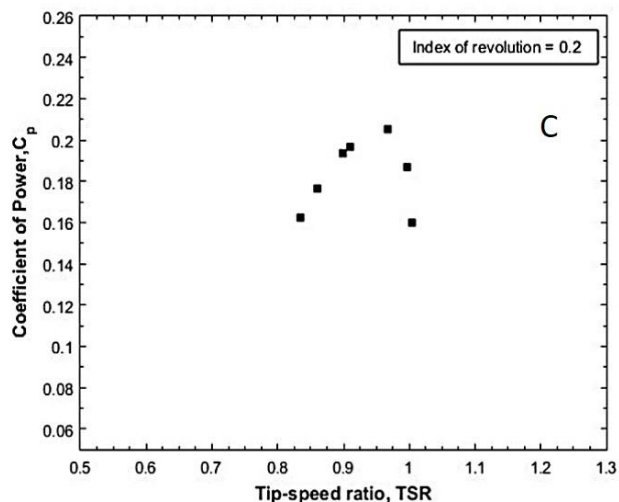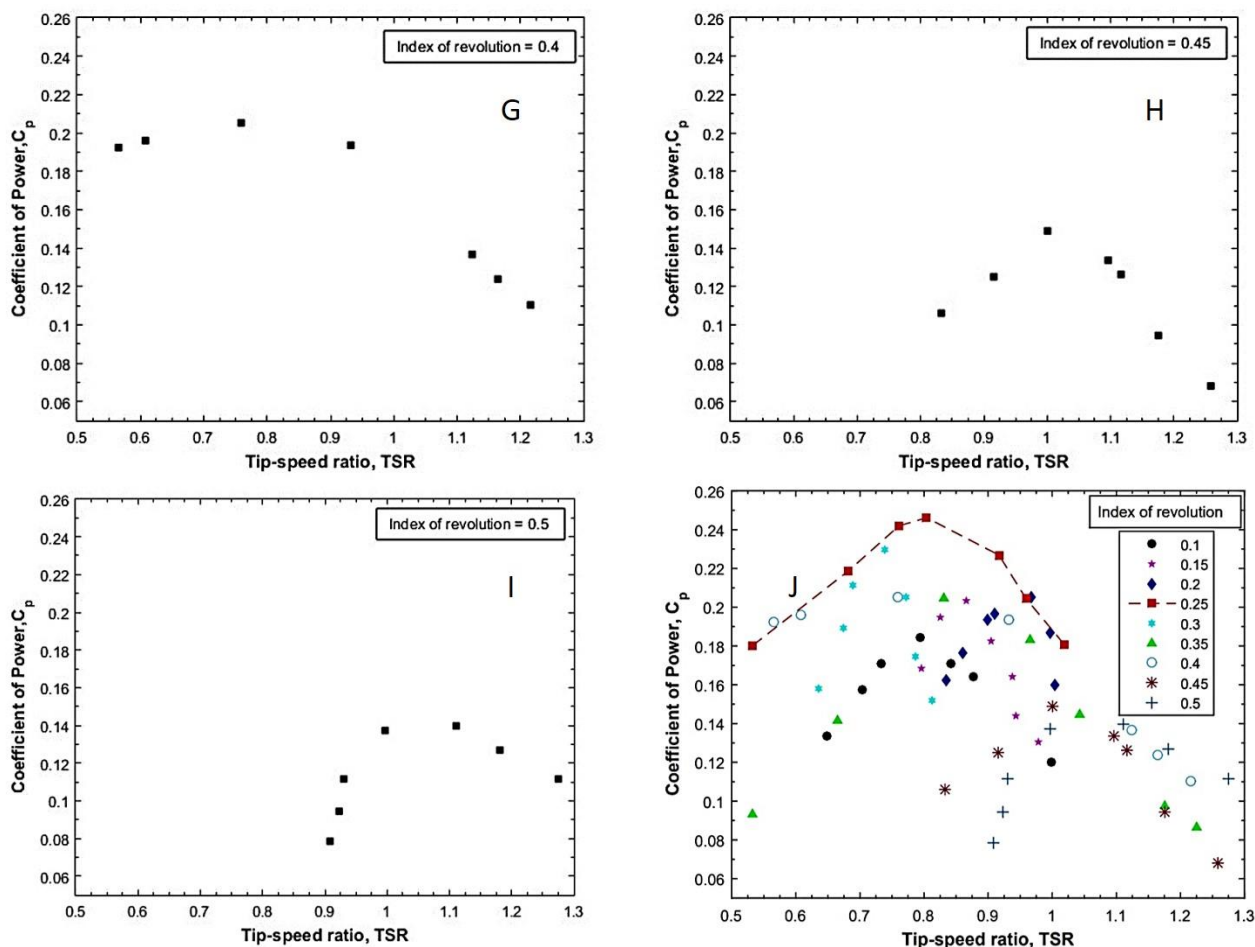
Fig. 15. (A-J) Variation of C_p with respect to TSR (Indices of revolution 0.1-0.5)

Figure 15(A-J) shows that TSR varies between 0.525 and 1.275, whereas C_p varies between 0.06 and 0.24. It is evident from Figure 15 (J) that the GHT with 0.25 as the index of revolution is the best in class, as the average C_p is much above that of other GHTs. The C_p Vs TSR plots demonstrated typical patterns found in Talukdar et al. [7] and Peter Bachant et al. [15, 34] investigations.

7.1.2 Velocity and pressure contours of GHT

Figure 16 illustrates the variation in the linear velocity of the fluid in the direction of flow relative to the turbine. The plot depicts the GHT with an index of revolution of 0.25. The flow lines near the turbine exhibit a significant change in velocity, which is consistent with expectations. This implies that the turbine blades use the fluid's dynamic pressure. Figure 16 illustrates the top plane (XY plane) and side plane (YZ plane). The planes considered for the velocity plot (as shown in Figure 17 A-I) are the top and side midplanes, and the direction of fluid flow is marked in the Y direction.
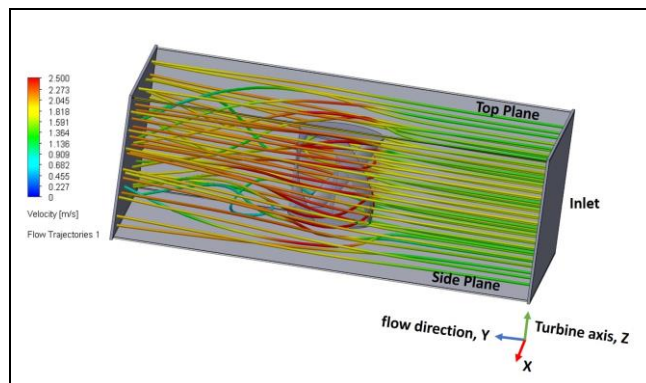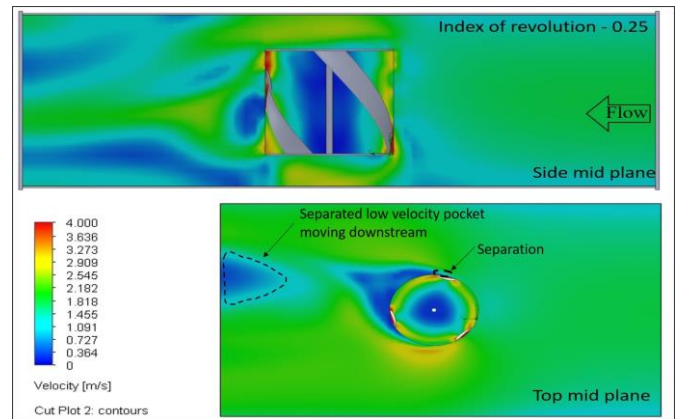

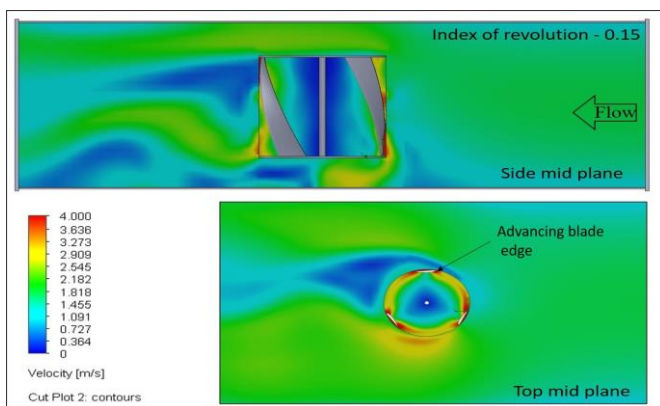**Fig. 16.** Linear velocity plots of the turbine with 0.25 as the index of revolution.

The velocity contours for GHTs with indices of revolution ranging from 0.1 to 0.5 subjected against 1.5 m/s are illustrated in Figure 17 A-I.
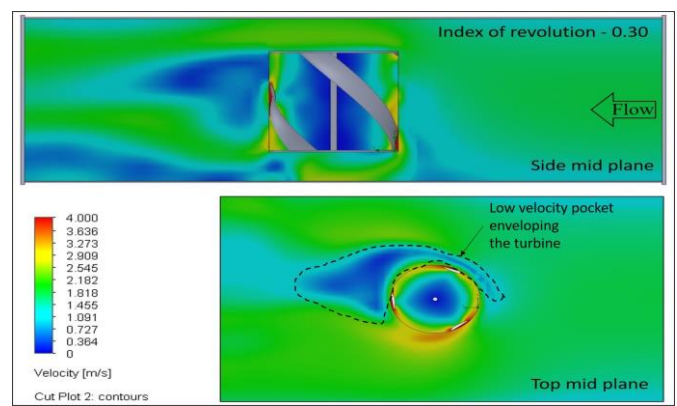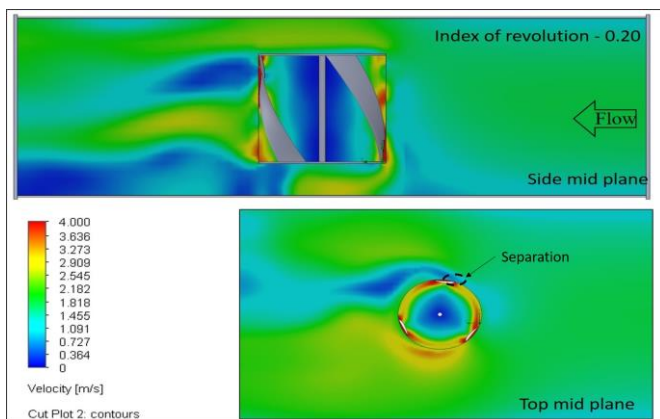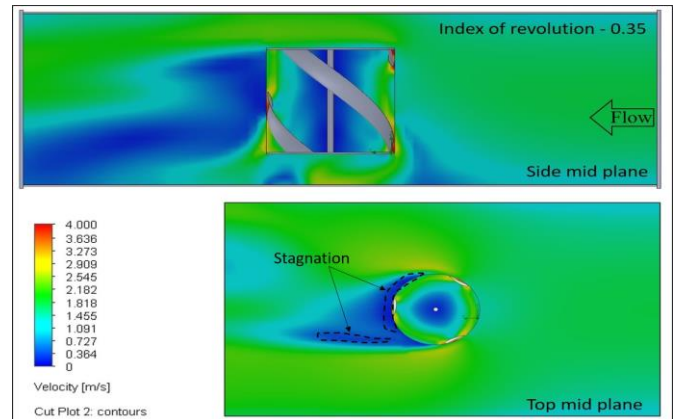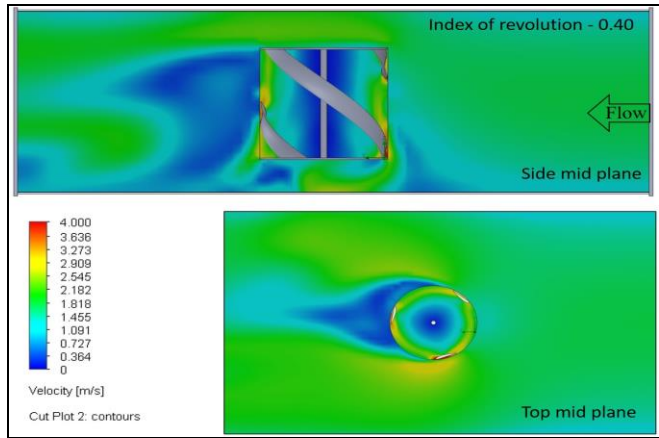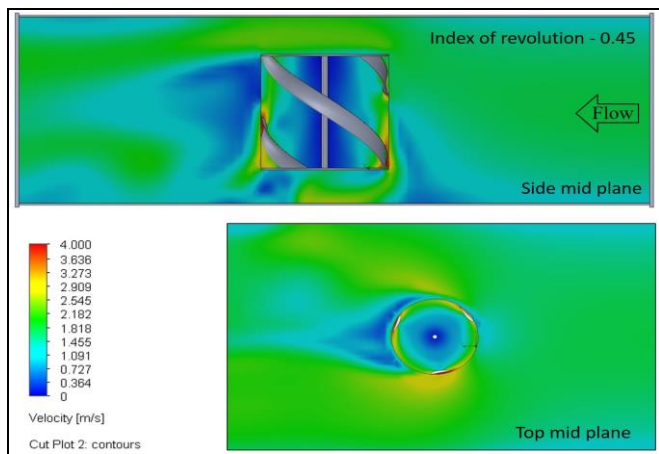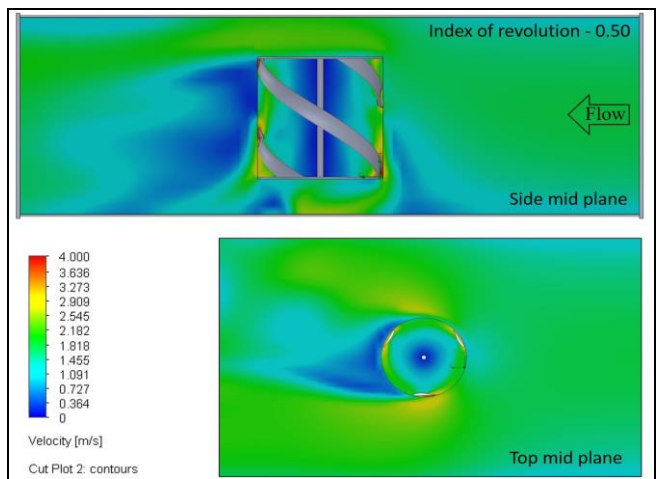
(A)

(B)

(C)

(D)

(E)
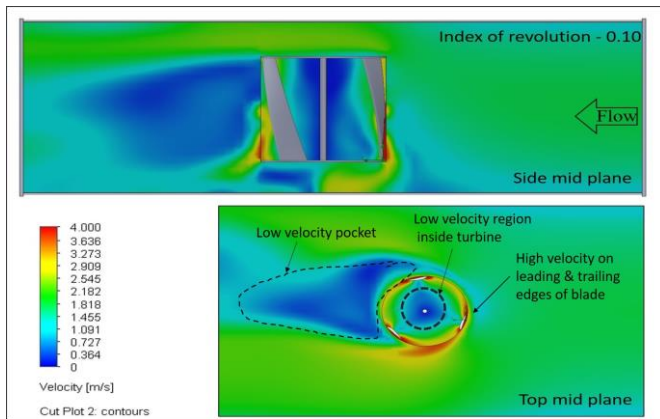
(F)

(G)

(H)

(I)

Fig. 17. (A-I) Velocity contour plots of GHT with different indices of revolution (0.10-0.50) for a flow velocity of 1.5 m/s

For GHTs with the indices of revolution of 0.10 and 0.15, the velocity contour (Figure 17 A, B) suggests that the GHT behaves more like a Darrieus turbine. For GHT with an index of revolution of 0.10, a low-velocity pocket is formed on the rear portion of the turbine. A similar low-velocity pocket can be observed inside the turbine. The velocity variations are also observed along the blades. Higher velocity can be observed on the leading and trailing edges of the turbine blades. These flow anomalies may result in flow-induced vibrations. Flow separation is observed on the advancing blades of turbines with indices of revolution 0.15, 0.20 and 0.25. A separated low-velocity pocket can be observed on GHT with an index of revolution of 0.25. This low-velocity pocket is completely separated from the low-velocity pocket occurring on the rear portion of the turbine, and it is found to move downstream of the flow (Figure 17 D).

For the GHT with an index of revolution of 0.30, a low-velocity pocket envelops more than half of the turbine circumference (Figure 17 E). Stagnation points occur on the rear section of the GHT with an index of revolution of 0.35 (Figure 17 F). As a result, the optimum range is reduced to GHTs with indices of revolution of 0.20 to 0.30. (Figure 17 C-E). The velocity plot of GHT with an index of revolution of 0.25 is the desired one. The fluid velocity is maximum at the leading edges. The low-velocity pockets are formed further away from the turbine. This flow pattern suggests that the GHT rotates smoothly and effectively, as the front edge is exposed to greater flow velocity while the trailing blades are in a lower velocity pocket.

Figure 18 illustrates the dynamic pressure variation in the direction of the fluid flow relative to the turbine. The plot depicts the GHT with an index of revolution of 0.25. Figure 18 illustrates the top plane (XY plane) and side plane (YZ plane). The planes considered for the pressure plot (as shown in Figure 19 A-I) are the top and side midplanes, and the direction of fluid flow is marked in the Y direction.
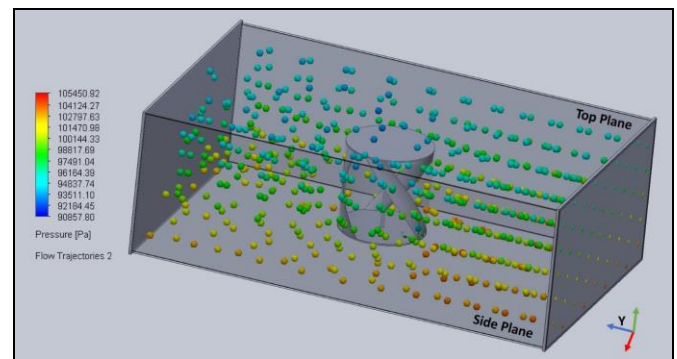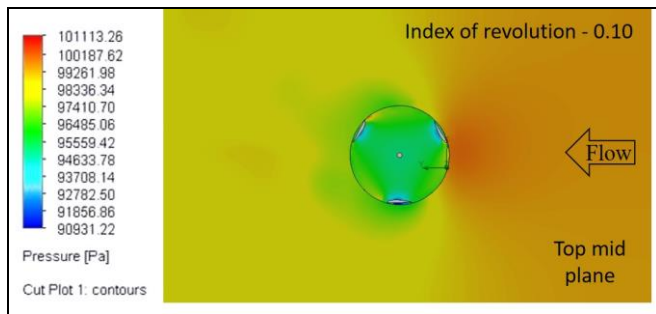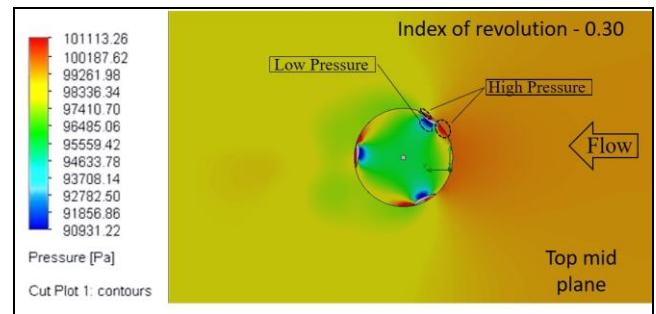

Fig. 18. Trajectory and dynamic pressure plot of the turbine with 0.25 as the index of revolution.
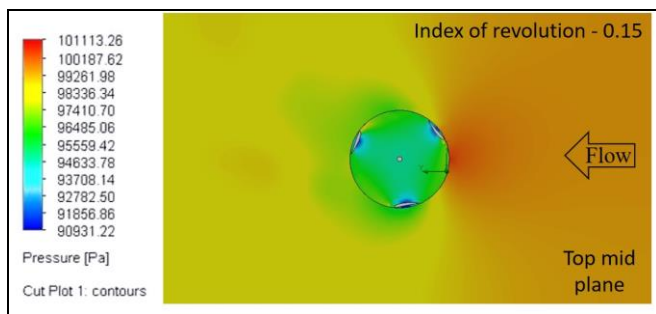
The total pressure contours for GHTs with indices of revolution ranging from 0.1 to 0.5 subjected against 1.5 m/s are illustrated in Figure 19 A-I.
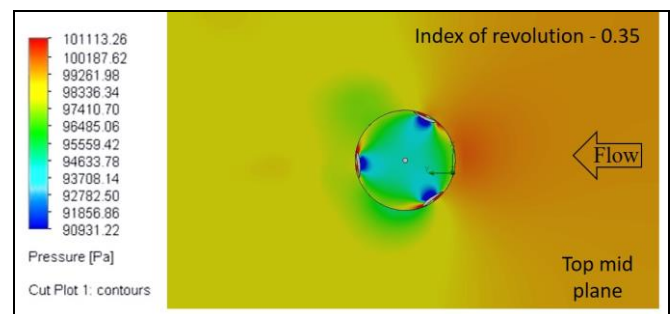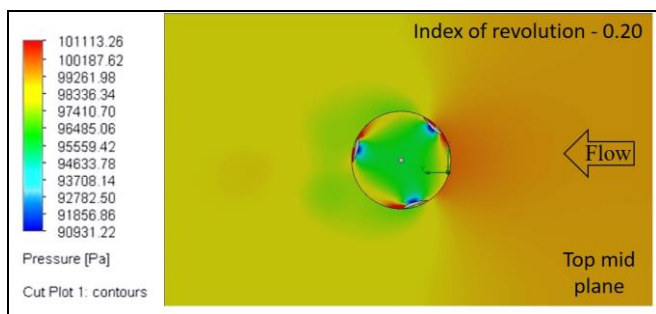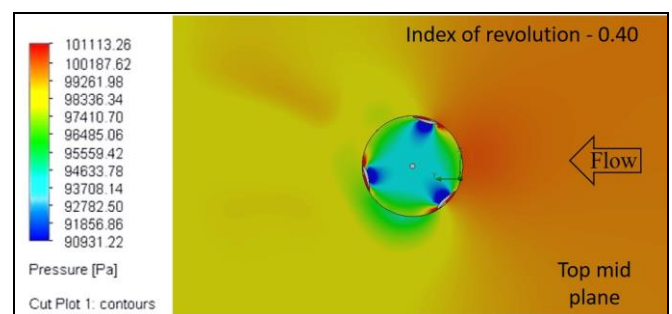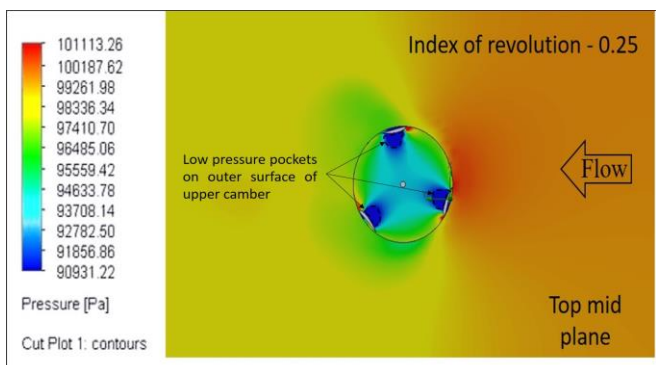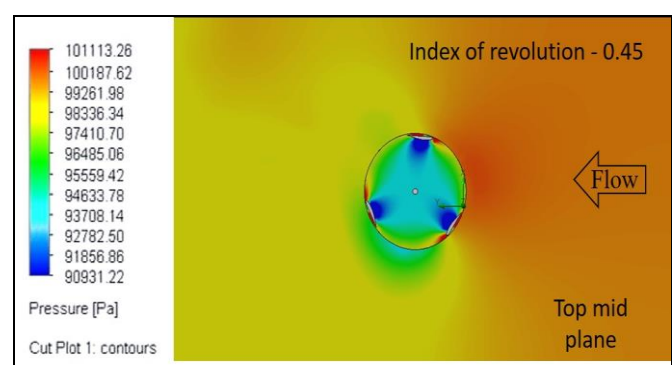
(A)

(B)

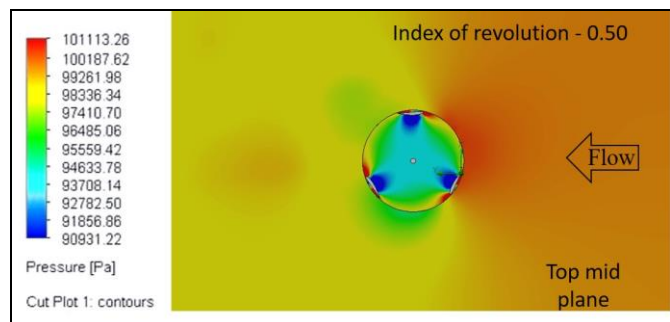(C)

(D)

(E)

(F)

(G)

(H)

(I)

Fig. 19. (A-I) Total pressure contour plots of GHT with different indices of revolution (0.10-0.50) for a flow velocity of 1.5 m/s

A decrease in total pressure across the turbine is noticed in all conditions. This pressure loss is transformed into the turbine's kinetic energy. On the leading surface of GHT blades with indices of revolution of 0.1 and 0.15, low-pressure pockets are observed (refer to Figures 19 A, B). As GHT is classified as a lift-based turbine, the significant share of the torque is attributed to the pressure difference between the leading and trailing edge of the blade. For turbines with an index of revolution of 0.20, a build-up of pressure at the leading edge is observed (refer to Figure 19 C). However, the pressure on the blades' trailing surface is not in order to develop a significant torque.

For GHT with an index of revolution of 0.25, the pressure drop across the leading and trailing edges is the most significant. According to these pressure contours (Figure 19 D), the turbine with a 0.25 index of revolution is the best in class. For GHTs with indices of revolution greater than 0.30 (Figure 19 E-I), a high-pressure pocket can be seen on the leading, trailing, and lower camber of the blade (Figure19 E). A low-pressure pocket is observed in the upper camber of the blade. Such a pressure pattern destabilises the blades' mechanical stability and induces bending stress.

7.2 Results from experimentation

Nine GHT models with different indices of revolution ranging from 0.10 to 0.50 were investigated using computational techniques. The GHT with an index of revolution of 0.25 was deemed suitable for the prototype. The experimental findings are summarised in Table 5 of Section 5.3. The turbine could self-start and produce energy when inserted into the river stream. Four runs were performed with a total duration clocking three hours. The turbine had the highest output power during the initial run. However, the output power reduced marginally in subsequent runs due to wakes and turbulence in the field caused by external agents. The power produced by the turbine in closed-form (analytical), simulation and experimental is compared in Table 8. In field-testing, the prototype delivered 0.65 W, 30% less than the figure calculated by simulation. The mismatch is exacerbated by the mechanical loss [35], profile shape, and

weight. Using parametric modelling and an associated technique, such as a genetic algorithm, to optimise multiple parameters might provide further insight into this problem [36]. The analyses point to a realistic solution for the struggling SHP segment based on tailrace and runoff water. Integrating intelligent grids [39-42] into these areas is critical.

Table 8. Comparison of output power

Index of revolution	Output power		
	Analytical	Simulation	Experimentation
0.25	1.11 W	0.951 W	0.65 W

8. Conclusion

The research aimed to investigate the GHT's parametric optimisation in terms of the index of revolution. A computational simulation was used to examine the influence of the index of revolution on the turbine's output power, which was then confirmed by experimental. The following are the outcomes of the research:

(1) According to studies, altering the helical blades' index of revolution affects the GHTs output power. GHT with an index of revolution of 0.25 is more efficient than other models.

(2) For flow velocity ranging from 1.1 m/s to 1.7 m/s, the coefficient of power values for GHT with 0.25 as the index of revolution was more significant than other turbines.

(3) S Shiono et al. confirmed that the force on the blade increases with helical angle. It is understood from Table 1 that the turbine with an index of revolution of 0.25 has a helical angle of 60°. U. Divakaran et al. suggested that the GHT with a helical angle of 60° performed exceptionally well compared to GHTs with other values of helical angle.

(4) The blade overlap angle corresponding to GHT with an index of revolution of 0.25 is 90.1° and is believed to be the optimum value. Philip Marsh et al. did not include this value (90.1°) in their computational analysis and ended with a notion that the performance degraded with the blade overlap angle. However, the current studies suggest an optimum value for the blade overlap angle.

(5) The GHT with an Index of revolution of 0.25 demonstrated a desirable velocity profile. For GHT with an index of revolution of 0.25, the pressure drop across the leading and trailing edges is the most significant and hence pronounced as the best in class. For all other GHTs, pressure gradients are observed along with the upper and lower camber of the blade. This pressure pattern destabilises the blades' mechanical stability and induces bending stress.

(6) The GHTs output power was computed analytically using Gavasheli's technique. As per the analytical calculation, the output power of GHT was 1.11 W, and that of the simulation was 0.951 W. The prototype generated 0.65 W at a flow velocity of 1.5 m/s, 30% less than the simulated result. Mechanical loss, external agents in field-testing, and inaccuracy in blade profile are attributed to the mismatch.

Acknowledgements

Abbreviations

GHT- Gorlov Helical Turbine.

SHP- Small Hydro Power plant.

H-Darrieus- Horizontal axis Darrieus water turbine.

NACA- National Advisory Committee for Aeronautics.

TSR- Tip Speed Ratio.

AR- Aspect Ratio.

FSM- Flow Simulation Module.

QUAD- Four Nodes quadrilaterals or hexahedral elements.

FVM- Finite volume method.

NS- Navier-Stokes equation.

RANS- Reynold Averaged Navier-Stokes

CR- Cold Rolled.

3D- Three-dimensional.

VAWT-Vertical Axis Wind Turbine

CG- Centre of Gravity

MOI- Momentt of Inertia

Nomenclature

φ – Helical angle.

β – Blade overlap angle.

σ – Relative solidity.

n, N–   Denotes the number of blades.

b – Chord of each blade cross-section, m.

D – Diameter of the turbine, m.

H – Height of the turbine, m.

P – Pitch of helix, m.

r – Radius of the turbine, m.

d – Half of the blade's chord in radians with respect to the axis of rotation, rad.

C_L – Coefficient of Lift as per NACA.

C_d – Coefficient of drag as per NACA.

C_p- Coefficient of power

α – Angle of attack.

ρ – Density of water, kg/m^3.

A – Projected area of the turbine, m^2.

V_f – velocity of the fluid, m/s.

V – Voltage, V.

F–Tangential force on the turbine, N.

T– Torque developed by the turbine, N m.

λ – Tip speed ratio (TSR).

ω – Angular velocity of the turbine, rad/s.

P – Power developed by the turbine, W.

I_t – Turbulence Intensity.

I – Current, A.

l –Turbulence length scale, m.

Re– Reynolds number.

K – Turbulent kinetic energy, m^2/s^2.

ε – Turbulence dissipation rate, m^2/s^3.

C_μ – Empirical constant, having an approximate value of 0.09.

References

[1] G. R. Mwaniki, M. O. Okok, and E. Oromat, "Expanding access to clean energy in developing countries: The role of off-grid mini hydro power projects in Kenya," *Int. J. Renew. Energy Res.*, vol. 9, no. 3, pp. 1571–1577, 2019, doi: 10.20508/ijrer.v9i3.9486.g7746.

[2] R. Alipour, R. Alipour, F. Fardian, S. S. R. Koloor, and M. Petrů, "Performance improvement of a new proposed Savonius hydrokinetic turbine: a numerical investigation," Energy Reports, vol. 6, pp. 3051–3066, 2020, doi: 10.1016/j.egyr.2020.10.072.

[3] S. Yagmur, F. Kose, and S. Dogan, "A study on performance and flow characteristics of single and double H-type Darrieus turbine for a hydro farm application," Energy Convers. Manag., vol. 245, no. August, p. 114599, 2021, doi: 10.1016/j.enconman.2021.114599.

[4] K. E. Okedu and M. Al-hashmi, "Assessment of the Cost of various Renewable Energy Systems to Provide Power for a Small Community: Case of Bukha, Oman," Int. J. Smart grid, vol. 3, no. 3, pp. 172–182, 2018, doi: 10.20508/ijsmartgrid.v2i3.17.g17.

[5] A. M. Gorlov, "Helical turbines for the gulf stream: conceptual approach to design of a large-scale floating power farm". Marine Technology and SNAME News. Vol.35, No.03, pp.175–182, 1998, doi:10.5957/mt1.1998.35.3.175.

[6] M. Shiono, K. Suzuki, and S. Kiho, "Output Characteristics of Darrieus Water Turbine with Helical Blades for Tidal Current Generations," Proc. Int. Offshore Polar Eng. Conf., vol. 12, pp. 859–864, 2002.

[7] P. K. Talukdar, V. Kulkarni, and U. K. Saha, "Field-testing of model helical-bladed hydrokinetic turbines for small-scale power generation," Renew. Energy, vol. 127, pp. 158–167, 2018, doi: 10.1016/j.renene.2018.04.052.

[8] S. Pongduang, C. Kayankannavee, and Y. Tiaple, "Experimental Investigation of Helical Tidal Turbine Characteristics with Different Twists," vol. 79. Elsevier B.V., 2015.

[9] B. K. Kirke, "Tests on ducted and bare helical and straight blade Darrieus hydrokinetic turbines," Renew. Energy, vol. 36, no. 11, pp. 3013–3022, 2011, doi: 10.1016/j.renene.2011.03.036.

[10] M. Mosbahi, A. Ayadi, Y. Chouaibi, Z. Driss, and T. Tucciarelli, "Experimental and numerical investigation of the leading edge sweep angle effect on the performance of a delta blades hydrokinetic turbine," Renew. Energy, vol. 162, pp. 1087–1103, 2020, doi: 10.1016/j.renene.2020.08.105.

[11] M. Mosbahi, A. Ayadi, Y. Chouaibi, Z. Driss, and T. Tucciarelli, "Performance improvement of a novel combined water turbine," Energy Convers. Manag., vol. 205, no. September 2019, p. 112473, 2020, doi: 10.1016/j.enconman.2020.112473.

[12] S. C M, R. Honnasiddaiah, V. Hindasageri, and V. Madav, "Experimental and numerical investigation of novel V-shaped rotor for hydropower utilization," Ocean Eng., vol. 224, no. April 2020, p. 108689, 2021, doi: 10.1016/j.oceaneng.2021.108689.

[13] S. C M, R. Honnasiddaiah, V. Hindasageri, and V. Madav, "Studies on application of vertical axis hydro turbine for sustainable power generation in irrigation channels with different bed slopes," Renew. Energy, vol. 163, pp. 845–857, 2021, doi: 10.1016/j.renene.2020.09.015.

[14] S. C M and V. Madav, "Numerical and experimental investigation of modified V-shaped turbine blades for hydrokinetic energy generation," Renew. Energy, vol. 177, pp. 1170–1197, 2021, doi: 10.1016/j.renene.2021.05.086.

[15] P. Bachant and M. Wosnik, "Helical Cross-Flow Axis Hydrokinetic Turbines, Including Effects of Waves and Turbulence," Proc. ASME-JSME-KSME 2011 Jt. Fluids Eng. Conf., pp. 1–12, 2011.

[16] R. Supreeth, A. Arokkiaswamy, N. J. Raikar, and H. P. Prajwal, "Experimental investigation of performance of a small scale horizontal axis wind turbine rotor blade," Int. J. Renew. Energy Res., vol. 9, no. 4, pp. 1983–1994, 2019.

[17] J. Zanette, D. Imbault, and A. Tourabi, "A design methodology for cross flow water turbines," Renew. Energy, vol. 35, no. 5, pp. 997–1009, 2010, doi: 10.1016/j.renene.2009.09.014.

[18] J. Anderson et al., "Design and Manufacture of a Cross-Flow Helical Tidal Turbine," 2011. [Online]. Available: http://depts.washington.edu/pmec/docs/20110615_ME495_report_Micropower.pdf.

[19] A. M. Gorlov, "The helical turbine: A new idea for low-head hydropower," Hydro Review. Vol 14, No-5, pp. 44-50. 1995.

[20] V. Jayaram and B. Bavanish, "Viability study of implementing cross flow helical turbine for micropower generation in India," Int. J. Renew. Energy Res., vol. 8, no. 1, pp. 274–279, 2018.

[21] V. Jayaram and B. Bavanish, "A brief review on the Gorlov helical turbine and its possible impact on power generation in India," Mater. Today Proc., vol. 37, no. Part 2, pp. 3343–3351, 2020, doi: 10.1016/j.matpr.2020.09.203.

[22] M. Camocardi, J. Marañón, J. Delnero, and J. Colman, "Experimental Study of a Naca 4412 Airfoil with Movable Gurney Flap," 2011, vol. 47, no. January, pp. 1–15, doi: 10.2514/6.2011-1309.

[23] A. Rezaeiha, I. Kalkman, and B. Blocken, "CFD simulation of a vertical axis wind turbine operating at a moderate tip speed ratio: Guidelines for minimum domain size and azimuthal increment," Renew. Energy, vol. 107, pp. 373–385, 2017, doi: 10.1016/j.renene.2017.02.006.

[24] M. A. Al-Dabbagh and M. I. Yuce, "Simulation and comparison of helical and straight-bladed hydrokinetic turbines," Int. J. Renew. Energy Res., vol. 8, no. 1, pp. 504–513, 2018.

[25] M. A. Al-Dabbagh and M. I. Yuce, "Numerical evaluation of helical hydrokinetic turbines with different solidities under different flow conditions," Int. J. Environ. Sci. Technol., vol. 16, no. 8, pp. 4001–4012, 2019, doi: 10.1007/s13762-018-1987-1.

[26] Z. Driss, O. Mlayeh, D. Driss, M. Maaloul, and M. S. Abid, "Numerical simulation and experimental validation of the turbulent flow around a small incurved Savonius wind rotor," Energy, vol. 74, no. C, pp. 506–517, 2014, doi: 10.1016/j.energy.2014.07.016.

[27] B. L. De Oliveira and J. Sundnes, "Comparison of tetrahedral and hexahedral meshes for finite element simulation of cardiac electro-mechanics," ECCOMAS Congr. 2016 - Proc. 7th Eur. Congr. Comput. Methods Appl. Sci. Eng., vol. 1, no. June, pp. 164–177, 2016, doi: 10.7712/100016.1801.9193.

[28] S. M. Letchumanan, A. M. Tajul Arifin, I. Taib, M. Z. Rahim, and N. A. Nor Salim, "Simulating the Optimization of Carbon Fiber Reinforced Polymer as a Wrapping Structure on Piping System Using SolidWorks," J. Fail. Anal. Prev., vol. 21, no. 6, pp. 2038–2063, 2021, doi: 10.1007/s11668-021-01287-4.

[29] R. Ragoth Singh and M. Nataraj, "Design and analysis of pump impeller using SWFS," World J. Model. Simul., vol. 10, no. 2, pp. 152–160, 2014.

[30] L. Prabhu, S. Krishnamoorthi, P. Gokul, N. Sushan, P. H. Hisham Harshed, and A. Jose, "Aerodynamics analysis of the car using solidworks flow simulation with rear spoiler using CFD," IOP Conf. Ser. Mater. Sci. Eng., vol. 993, no. 1, 2020, doi: 10.1088/1757-899X/993/1/012002.

[31] A. Akhatova, A. Kassymov, M. Kazmaganbetova, and L. Rojas-Solórzano, "CFD simulation of the dispersion of exhaust gases in a traffic-loaded street of Astana, Kazakhstan," J. Urban Environ. Eng., vol. 9, no. 2, pp. 158–166, 2015, doi: 10.4090/juee.2015.v9n2.158166.

[32] M. A. Price and C. G. Armstrong, "Hexahedral mesh generation by medial surface subdivision: Part ii. solids with flat and concave edges," Int. J. Numer. Methods Eng., vol. 40, no. 1, pp. 111–136, 1997, doi:10.1002/nme.1620381910.

[33] R. J. Moffat, "Describing the uncertainties in experimental results," Exp. Therm. Fluid Sci., vol. 1, no. 1, pp. 3–17, 1988, doi: 10.1016/0894-1777(88)90043-X.

[34] P. Bachant and M. Wosnik, "Performance measurements of cylindrical- and spherical-helical cross-flow marine hydrokinetic turbines, with estimates of exergy efficiency," Renew. Energy, vol. 74, pp. 318–325, 2015, doi: 10.1016/j.renene.2014.07.049.

[35] Z. Yun, G. Y. Kun, Z. L. Xiang, X. T. Mao, and D. H. Kui, "Torque model of hydro turbine with inner energy loss characteristics," Sci. China Technol. Sci., vol. 53, no. 10, pp. 2826–2832, 2010, doi: 10.1007/s11431-010-4098-x.

[36] A. Pourrajabian, M. Dehghan, and S. Rahgozar, "Genetic algorithms for the design and optimization of horizontal axis wind turbine (HAWT) blades: A continuous approach or a binary one?" Sustain. Energy Technol.

Assessments, vol. 44, no. September 2020, p. 101022, 2021, doi: 10.1016/j.seta.2021.101022.

[37] U. Divakaran, A. Ramesh, A. Mohammad, and R. K. Velamati, "Effect of helix angle on the performance of helical vertical axis wind turbine," Energies, vol. 14, no. 2, pp. 1–24, 2021, doi: 10.3390/en14020393.

[38] P. Marsh, D. Ranmuthugala, I. Penesis, and G. Thomas, "Numerical investigation of the influence of blade helicity on the performance characteristics of vertical axis tidal turbines," Renew. Energy, vol. 81, pp. 926–935, 2015, doi: 10.1016/j.renene.2015.03.083.

[39] A. T. Boum and C. F. Mbey, "Optimal Reliability of a Smart Grid," Int. J. Smart grid, vol. 5, no. 2, 2021, doi: 10.20508/ijsmartgrid.v5i2.182.g149.

[40] U. Cetinkaya and R. Bayindir, "On&Off-Grid Hybrid Microgrid Design and Dynamic Analysis,"

2019 7th International Conference on Smart Grid (icSmartGrid), 2019, pp. 132-136, doi: 10.1109/icSmartGrid48354.2019.8990881.

[41] M. I. Abid, M. S. Khalid, M. Kamran, M. Arshad, M. F. Masood, and T. Murtaza, "Design and Optimization of the Micro- Hydro Power System for Remote Areas of Pakistan," Int. J. Smart grid, vol. 4, no. 3, 2020, doi: 10.20508/ijsmartgrid.v4i3.107.g100.

[42] F. Ayadi, I. Colak, I. Garip, and H. I. Bulbul, "Targets of Countries in Renewable Energy," 9th Int. Conf. Renew. Energy Res. Appl. ICRERA 2020, pp. 394–398, 2020, doi: 10.1109/ICRERA49962.2020.9242765.